Modeling, Analysis and Testing of Load Distribution for Planetary Gear Trains with 3D Carrier Pinhole Position Errors

Dong, Huimin; Zhang, Chu ; Bai, Shaoping; Wang, Delun

Published in:
International Journal of Precision Engineering and Manufacturing

DOI (link to publication from Publisher):
10.1007/s12541-019-00166-1

Publication date:
2019

Document Version
Accepted author manuscript, peer reviewed version

DOI: XXX-XXX-XXXX

Modeling, Analysis and Testing of Load Distribution for Planetary Gear Trains with 3D Carrier Pinhole Position Errors

Huimin Dong[1,#], Chu Zhang[1], Shaoping Bai[2] and Delun Wang[1]

1 School of Mechanical Engineering, Dalian University of Technology, Dalian, 116-024, China
2 Department of Mechanical and Manufacturing Engineering, Aalborg University,DK-9220 , Denmark
Corresponding Author / E-mail: donghm@dlut.edu.cn

KEYWORDS : Planetary gear train, Load distribution, Carrier pinhole errors, Discrete method

A discrete model to study the load distribution behavior of helical planetary gear trains (PGTs) is developed, in which 3D planet position errors, induced by carrier pinhole position errors and tooth modifications, are duly considered. The model adopts a discrete approach with which the planetary gear train is discretized into a series of slice-units in order to ease the problem of gear meshing in 3D cases. In the modelling, compatibility conditions and discrete equilibrium are developed for the coupling among 3D planet position errors, tooth modifications, instantaneous meshing situations, elastic deformations and rigid body spatial motions. Upon the discrete model, a method for analysis of the load distribution is further developed. The influence of 3D planet position errors and tooth modifications on the load distribution was simulated for a helical PGT having three and four planets. Tests on the actual wind turbine PGTs were conducted with results agreed with the simulations obtained, which validate the proposed method.

Manuscript received: XX, 201X / Accepted: XX, 201X

NOMENCLATURE

N = number of planet gears
N_s, N_p, N_r = number of teeth of the sun, planet and ring gear
$\boldsymbol{i}$, $\boldsymbol{j}$, $\boldsymbol{k}$ = unit vector of Cartesian axes X,Y,Z
$\boldsymbol{S}$ = fixed coordinate system
$\boldsymbol{s}$ = moving coordinate system
ψ_{pi} = planet position angle
ξ_r, ξ_t = radial, tangential parallel misalignment error
ζ_r , ζ_t = radial, tangential angular misalignment error
l, Δl = gear width, thickness of the slice-unit
n_l = number of slice-units
β, r, s = helix angle, radius and tooth thickness of base circle
p_b = base pitch
$\boldsymbol{r} = (x, y, z)^{\mathrm{T}}$ = point vector
$\boldsymbol{n}$ = unit normal vector of tooth surface
$\boldsymbol{M}$, $\boldsymbol{R}$, $\boldsymbol{L}$ = matrix of coordinate transformation
κ_s = rotating direction of the sun gear
θ = rotation angle
ω= angular velocity
a = center distance
$\boldsymbol{a}_i$ = position vector for the i-th planet center
α = transverse operating pressure angle
σ = tooth modification amount
e = clearance of the meshing gear pair
$\Delta\boldsymbol{r}$, $\Delta\varphi$ = deviation of the contact position and rotation angle
$\boldsymbol{\delta}$, δ = vector and scalar of elastic deformation
$\boldsymbol{x}$, $\boldsymbol{u}$ = vector of translational and rotational displacement
k, c = stiffness and damping of meshing and supporting
L_{pi} = load distribution coefficient of the i-th planet
C = maximum deviation of tooth modification
$\boldsymbol{F}$, $\boldsymbol{T}$ = vector of force and torque
$\boldsymbol{m}$, $\boldsymbol{q}$ = matrix of mass and displacement
$\boldsymbol{k}_\omega$, $\boldsymbol{k}_h$ = matrix of centripetal and supporting stiffness
$\boldsymbol{G}$, $\boldsymbol{c}_h$ = matrix of gyroscopic and supporting damping
ε = peak-to-peak microstrain of the tooth root

Subscripts/ Superscripts:
c, s, r = carrier, sun gear, ring gear
pi = the i-th planet gear
P = pitch point
0 = initial position
n = number of the contact tooth pairs
Ei = the i-th external meshing gear pair
Ii = the i-th internal meshing gear pair

1. Introduction

The load distribution is a major concern for heavy-duty planetary gear trains (PGTs) that are used in automotive, aeronautical, wind energy and power transmission industries. The inevitable manufacturing and assembly errors will cause undesirable load distribution in the PGTs, which implies that the load is not equally shared among the different sun/planet/ring branches and along the gear face width. This will affect the life duration and dynamic behavior of PGTs.

Many research works on the load distribution problem of PGTs are available in literatures[1-19], with approaches including finite element method[1-2], analytical method[3-15], analytical-FE method[16-17] and experimental method[18-20], to address the load distribution performance under the influences of manufacturing and assembly errors. The finite element method is accurate and comprehensive by including elasticity and different errors, but it demands significant computational effort.[1-2] The analytical method of lumped parametric model owns high computational efficiency, low cost and reasonable accuracy for the load distribution analysis if the instantaneous geometry between gears is accurate, and time-varying mesh stiffness is considered accordingly. A lumped parametric dynamic model of a PGT was first established by Saada and Velex in 1992 to investigate the tooth loading critical frequencies.[3] Kahraman established a dynamic model and put forward the concept of load sharing coefficient.[4] Velex analyzed three-dimensional tooth load behavior of a PGT by established 3D finite element/lumped parameter model without considering errors and time-varying mesh stiffness associated to the contact positions. It was pointed out that the effects of planet position errors should be investigated.[16]

The planar (2D) planet position errors were considered in the dynamic/load distribution modeling of PGTs.[5-15] Botman and Toda studied the influence of errors and found significant effects depending on planet position errors.[5] Bodas and Kahraman had made outstanding contribution to the influence of planar planet position errors on the load sharing performance.[6] Gu and Velex adopted a screw method to discuss the instantaneous gear geometry and investigated the influence of planet parallel misalignment on the load sharing.[7] Singh proposed a generalized formulation for the effects of planar planet position errors on load sharing behavior.[8] Dong established a multi-DOF dynamics model for PGT's load sharing analysis of which each gear center errors are taken into account.[10] Hu and Kahraman established the load distribution model of PGTs considering planar manufacturing and assembly errors.[11] Kim et al analyzed load sharing behavior considering planar carrier pinhole position errors with experimental validation.[13,19,20] Park investigated the effects of planar planet position errors and non-torque loads on load sharing behavior of wind turbine gearbox.[14] Cao and Shao established four-DOF dynamic and quasi-static model considering carrier misalignment error as a planar problem.[15] From the literature, it is noticed that there are very few papers about the influences of 3D planet position errors on PGT's load distribution behavior using analytical method.

Many approaches were proposed too to improve the load distribution behavior. [21-24] Litvin proposed the design approach of PGT with double-crowned modification for improving conditions of load distribution among the planet gears.[21] Mohamad studied convex modification of tooth flank considering elastic deformation under load.[22] Oh analyzed the transmission error of a helical gear pair with the tooth microgeometry optimized.[23] Kim adopted instant screw axis and finite element method for calculating tooth modification amount of a wind turbine gearbox.[24] In these work mentioned, the main factor addressed is the gear tooth profile and elastic deformation, while the 3D planet position errors are not included in the modeling and design analysis yet. For this reason, the coupling effects of 3D planet position errors and tooth modification on the load distribution of PGTs are unrevealed. A rigorous and effective modeling method considering tooth modifications and 3D planet position errors, involving parallel and angular misalignment, is thus needed.

In this paper, a discrete model of PGTs having an arbitrary number of planets is developed. The PGT is discretized into a series of slice-units along axial direction, and the instantaneous gear geometry/ kinematics for each slice-unit is explicitly depicted to reveal the actual meshing situations of gear pairs. The discrete model is coupled with 3D planet position errors, tooth modifications, instantaneous mesh statuses, elastic deformations and rigid body motions with six-DOF through establishing elastic compatibility equations. Upon the discrete model, a method for analysis of the load distribution is further developed. Simulations were conducted for a helical PGT with tooth modifications and 3D planet position errors. Tests on the actual wind turbine PGTs were performed. The results validate the method developed.

2. Description of 3D planet position errors and tooth modifications in a PGT

For an ideal PGT without carrier pinhole errors, all axes of planets are parallel, and planets can be equally or unequally distributed around the sun gear on the same cylindrical surface. In reality, due to the presence of manufacture and assembly errors, the axes of planets will deviate from their ideal positions, producing 3D planet position errors. The 3D position errors will cause the deviation of contact position and motion of gears from the ideal one, which will affect the PGT load distribution performance.

For convenience, the geometry and kinematics of a PGT are discussed in reference carrier frame $\boldsymbol{S}_C\{O; X_C, Y_C, Z_C\}$. The auxiliary reference frames $\boldsymbol{S}_{Pi}$ at each planet center, and the gear moving frame $\boldsymbol{s}_J$ ($J = s, r$) and $\boldsymbol{s}_{pi}$ ($i = 1,2,\ldots,N$) at each gear center are defined, as shown in Fig. 1, in which y-axis of $\boldsymbol{s}_J$ ($J = s, r, pi$) goes through the symmetric line of the first gear tooth. All X-Y planes are in the middle cross-section of the PGT.

3D planet position errors can be dissolved into the parallel misalignment and angular misalignment in the radial and tangential direction. The position errors are described in the auxiliary frame $\boldsymbol{S}_{Pi}$,

DOI: XXX-XXX-XXXX

shown in Fig. 2, in which the parallel misalignment is expressed by ξ_{ri} and ξ_{ti} along X_{Pi}-, Y_{Pi}-direction, and the angular misalignment by the rotational angle ζ_{ri} and ζ_{ti} about X_{Pi}-, Y_{Pi}-direction,

$$\boldsymbol{\xi}_i = \xi_{ri}\boldsymbol{i} + \xi_{ti}\boldsymbol{j}, \quad \boldsymbol{\zeta}_i = \zeta_{ri}\boldsymbol{i} + \zeta_{ti}\boldsymbol{j} \tag{1}$$

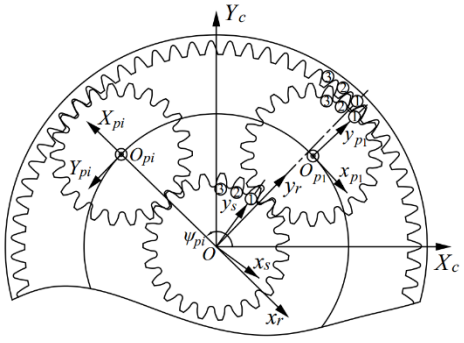

Fig. 1 Coordinate systems defined in middle cross-section of a PGT

The tooth modification is an effective method for compensating the negative effects of 3D planet position errors on load distribution. Generaly, the tooth modification includes tooth profile modification and lead modification. The amount of the modification $\sigma=f(u,z)$ in this paper is defined as the normal value of tooth surface, i.e. a function of parameters u and z respectively along transverse profile and gear-axis direction.

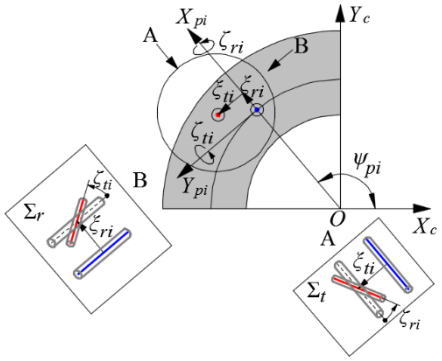

Fig. 2 A schematic of 3D planet position errors

As discussed before, 3D planet position errors, containing both parallel and angular misalignment, are coupled with tooth modifications, and make the meshing situations solving become extremely difficult for an overall PGT system with multi-planet as it is an over constraints 3D system. A discrete model for a PGT that is able to ease the determination of gear meshing conditions in the presence of both 3D position errors and tooth modifications on load distribution is thus developed in this work.

3. Description of discrete model of a PGT

3.1 Description of discrete geometric and kinematic model

To start with the geometric and kinematic modeling, the helical PGT is first discretized into a series of slice-units.

3.1.1 Slice-units and their tooth surfaces

The PGT with gear width l is discretized into n_l slice-units along the carrier axis, $j=1,2\ldots n_l$ counted from the front end face of each gear. Figure 3 illustrates the discrete geometry model of a branch of *sun-pi-ring*, in which $\boldsymbol{s}_{Jj}$ ($J=s, r, pi$) is the j-th slice-unit coordinate system at its front end face. The y-axis of each slice-unit system is coincident to the middle line of the first gear tooth.

According to the principle of involute helicoid surface generation, the relative angle about z-axis between $\boldsymbol{s}_J$ and $\boldsymbol{s}_{Jj}$ is

$$\Delta\beta_{J,j} = \left[l/2 - \Delta l\left(j-1\right)\right]\tan\beta_J / r_J, \quad J = s,r,pi \tag{2}$$

When number of slice-units is large enough, the thickness of a slice-unit $\Delta l = l/n_l$ is very small, the tooth profile of the front-end face of a slice-unit is employed to approximately describe the tooth surface of the unit, thereby, all tooth profiles of slice-units in a gear form the gear tooth surface.

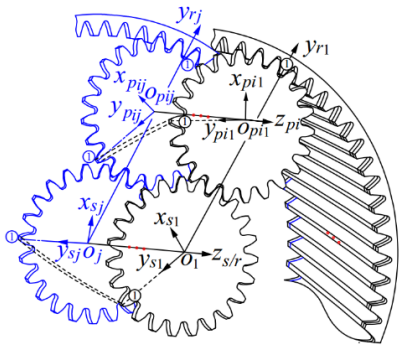

Fig. 3 A sun/planet/ring branch of the discretized PGT model

For an arbitrary slice-unit j, $j=1,2,\ldots n_l$, the tooth surfaces of each operating side in its own $\boldsymbol{s}_{Jj}$ system are given, for *sun-pi* external pair and *pi-ring* internal pair, as

$$\boldsymbol{r}^{E/Ii}_{J,j,m} = (x^{E/Ii}_{J,j,m}, y^{E/Ii}_{J,j,m}, 0)^{\mathrm{T}} \quad J = s,r,pi, \quad m = 1,\ldots N_{s/r/pi} \tag{3}$$

According to gearing theory, the involute equations in Eq. (3) can be expressed as

$$\begin{cases} x^{E/Ii}_{J,j,m} = r_J(\cos\tau^{E/I}_{J,m} \mp \kappa_s u \sin\tau^{E/I}_{J,m}) \\ y^{E/Ii}_{J,j,m} = r_J(\sin\tau^{E/I}_{J,m} \pm \kappa_s u \cos\tau^{E/I}_{J,m}) \end{cases} \quad J = s,pi,r \tag{4a}$$

where,
$$\begin{cases} \tau^{E}_{J,m} = \pi/2 + \kappa_s s_J / 2r_J - \kappa_s u + u_m, \ J = s, pi \\ \tau^{I}_{pi,m} = \pi/2 - \kappa_s s_{pi} / 2r_{pi} + \kappa_s u + u_m \\ \tau^{I}_{r,m} = \pi/2 + \kappa_s s_r / 2r_r - \kappa_s u + u_m \end{cases} \tag{4b}$$

$\kappa_s=1$ for the sun gear counter-clockwise rotating, otherwise $\kappa_s=-1$, u is the variable parameter, and $u_m=(m-1)p_b/r_J$.

The relationship between the j-th slice-unit and the moving coordinate systems of each gear can be expressed by transformation matrix $\boldsymbol{M}_{J,j}$ from the j-th slice-unit system $\boldsymbol{s}_{Jj}$ to the gear system $\boldsymbol{s}_J$,

$$\boldsymbol{M}_{J,j}=\boldsymbol{M}(\boldsymbol{R}(z,\Delta\beta_{J,j}),\boldsymbol{L}_{J,j})\quad J=s,pi,r \tag{5}$$

where $\boldsymbol{L}_{J,j}=(0,0,l/2-\Delta l(j-1))^{\mathrm{T}}$, and $\boldsymbol{R}(z,\Delta\beta_{J,j})$ is the rotation matrix about z-axis.

The tooth surfaces of the j-th slice-unit in Eq. (3) in $\boldsymbol{S}_C$ at any instant can be obtained by the transformation matrix, as

$$\begin{pmatrix}{}^{S_C}\boldsymbol{r}^{E/I}_{J,j,m}(t)\\1\end{pmatrix}=\boldsymbol{M}_{CJ}(t)\boldsymbol{M}_{J,j}\begin{pmatrix}\boldsymbol{r}^{E/I}_{J,j,m}\\1\end{pmatrix}\quad J=s,pi,r \tag{6}$$

where $\boldsymbol{M}_{CJ}(t)=\boldsymbol{M}(\boldsymbol{R}(z,\theta_{J0}+(\omega_J-\omega_C)t),\boldsymbol{L}_{CJ})$ is the transformation matrix from $\boldsymbol{s}_J$ to $\boldsymbol{S}_C$ system, $\boldsymbol{L}_{Cs/r}=\boldsymbol{0}$, $\boldsymbol{L}_{CPi}=\boldsymbol{a}_i$, and θ_{J0} are initial assembly angles, $\theta_{r0}=\psi_{p1}-\pi/2+p_b/2r_r$, $\theta_{pi0}=\psi_{p1}-\pi/2+(1-N_r/N_p)(\psi_{pi}-\psi_{p1})$, for even N_p, $\theta_{s0}=\psi_{p1}-\pi/2$, otherwise $\theta_{s0}=\psi_{p1}-\pi/2-p_b/2r_s$.

Equation (6) describes the geometry and kinematics of the tooth surface of an arbitrary slice-unit of gears at an instant t, which can be solved by using Eq. (2)-(6) in the same coordinate system.

3.1.2 Contact position and relative motion of each slice-unit gear pair

Under ideal condition, for *sun-planet/planet-ring* pair, let $\boldsymbol{r}^{E/Ii}_{P,j}$ and $\boldsymbol{n}^{E/Ii}_{P}$ in $\boldsymbol{S}_C$ system be the vector of pitch point and common normal direction of a unit-slice gear pair. They are given as

$$\begin{cases}\boldsymbol{r}^{E/Ii}_{P,j}=(a\dfrac{N_{s/r}}{N_{s/r}\pm N_p}\cos\psi_{pi},a\dfrac{N_{s/r}}{N_{s/r}\pm N_p}\sin\psi_{pi},\dfrac{l}{2}-(j-1)\Delta l)^{\mathrm{T}}\\ \boldsymbol{n}^{E/Ii}_{P}=\kappa_s(-\sin(\psi_{pi}\mp\kappa_s\alpha_{E/I}),\cos(\psi_{pi}\mp\kappa_s\alpha_{E/I}),0)^{\mathrm{T}}\end{cases} \tag{7}$$

The contact point of the *sun-pi/pi-ring* pair satisfies

$$\begin{cases}({}^{S_C}\boldsymbol{r}^{Ei}_{s,j,m}-\boldsymbol{r}^{Ei}_{P,j})\times\boldsymbol{n}^{Ei}_{P}=({}^{S_C}\boldsymbol{r}^{Ei}_{pi,j,m}-\boldsymbol{r}^{Ei}_{P,j})\times\boldsymbol{n}^{Ei}_{P}=0\\ ({}^{S_C}\boldsymbol{r}^{Ii}_{pi,j,m}-\boldsymbol{r}^{Ii}_{P,j})\times\boldsymbol{n}^{Ii}_{P}=({}^{S_C}\boldsymbol{r}^{Ii}_{r,j,m}-\boldsymbol{r}^{Ii}_{P,j})\times\boldsymbol{n}^{Ii}_{P}=0\end{cases} \tag{8}$$

From Eqs. (7)-(8), the contact positions of the external/internal meshing pair of *sun-pi/pi-ring* are obtained through traversing all the teeth at any instant. The number of the contact tooth pairs at the same time is recorded by n=1, 2,…, $n^{E/Ii}$.

By using Eqs. (6)-(8), the contact position ${}^{Sc}\boldsymbol{r}^{E/Ii}_{J,j,n}$ for the n-th contact tooth pair is uniquely determined. For the meshing pair, the contact position of any slice-unit also satisfies

$${}^{S_C}\boldsymbol{r}^{Ei}_{j,n}-\boldsymbol{M}^{-1}_{CPi}\,{}^{S_C}\boldsymbol{r}^{Ei}_{j,n}={}^{S_C}\boldsymbol{r}^{Ii}_{j,n}-\boldsymbol{M}^{-1}_{CPi}\,{}^{S_C}\boldsymbol{r}^{Ii}_{j,n}=\boldsymbol{a}_i \tag{9}$$

where $\boldsymbol{M}^{-1}_{CPi}$ is transformation matrix from $\boldsymbol{S}_C$ system to $\boldsymbol{S}_{Pi}$ system, shown in Appendix.

Figure 4 shows gear teeth meshing in a slice-unit gear pair. The tooth surface errors or profile modifications of each gear are expressed in the normal direction of tooth profiles, as $\sigma_{J,j}\boldsymbol{n}^{E/Ii}$.

Let $\Delta\boldsymbol{r}^{Ei}_{s,j,n}$, $\Delta\boldsymbol{r}^{E/Ii}_{pi,j,n}$ and $\Delta\boldsymbol{r}^{Ii}_{r,j,n}$ be the deviations of the contact position, $\Delta\varphi_{s,i,j,n}$ and $\Delta\varphi_{pi,j,n}$ ($\Delta\varphi_{r,i,j,n}$=0 due to the ring gear is fixed) be those of the rotation angle about Z-axis relative to the ideal one in any *sun-pi-ring*. The contact condition with consideration of only the first order small quantity satisfies:

$${}^{S_C}\boldsymbol{r}^{*Ei}_{j,n}-{}^{S_{Pi}}\boldsymbol{r}^{*Ei}_{j,n}={}^{S_C}\boldsymbol{r}^{*Ii}_{j,n}-{}^{S_{Pi}}\boldsymbol{r}^{*Ii}_{j,n}=\boldsymbol{a}_i+\boldsymbol{\xi}_i \tag{10}$$

$$\begin{cases}{}^{S_C}\boldsymbol{r}^{*E/Ii}_{j,n}={}^{S_C}\boldsymbol{r}^{E/Ii}_{j,n}+\Delta\boldsymbol{r}^{E/Ii}_{s/r,j,n}\mp\sigma_{s/r,j}\boldsymbol{n}^{E/Ii}+\Delta\varphi_{s/r,i,j,n}\boldsymbol{k}_c\times{}^{S_C}\boldsymbol{r}^{E/Ii}_{j,n}\\ {}^{S_{Pi}}\boldsymbol{r}^{*E/Ii}_{pi,j,n}={}^{S_{Pi}}\boldsymbol{r}^{E/Ii}_{j,n}+\Delta\boldsymbol{r}^{E/Ii}_{pi,j,n}\pm\sigma_{pi,j}\boldsymbol{n}^{E/Ii}\\ +\boldsymbol{\zeta}_i\times{}^{S_{Pi}}\boldsymbol{r}^{E/Ii}_{j,n}+\Delta\varphi_{pi,j,n}\boldsymbol{k}_{pi}\times{}^{S_{Pi}}\boldsymbol{r}^{E/Ii}_{j,n}\end{cases} \tag{11}$$

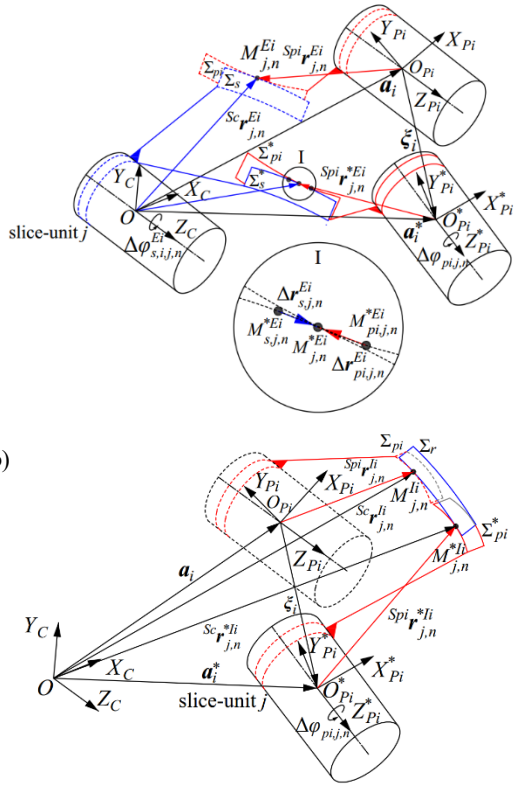

Fig. 4 Tooth pair mesh in a slice-unit with 3D planet position errors and tooth modification: (a) *sun-planet* pair; (b) *planet-ring* pair

Substituting Eq. (11) into Eq. (10) and multiplying both sides with unit normal vectors of tooth surface, $\boldsymbol{n}^{Ei}$ and $\boldsymbol{n}^{Ii}$, Eq. (10) becomes

$$(\Delta\varphi_{pi,j,n}\boldsymbol{k}_{pi}\times{}^{S_{Pi}}\boldsymbol{r}^{Ii}_{j,n}-\sigma_{r,j}\boldsymbol{n}^{Ii}-\sigma_{pi,j}\boldsymbol{n}^{Ii}+\boldsymbol{\zeta}_i\times{}^{S_{Pi}}\boldsymbol{r}^{Ii}_{j,n})\cdot\boldsymbol{n}^{Ii}=-\boldsymbol{\xi}_i\cdot\boldsymbol{n}^{Ii} \tag{12a}$$

$$\begin{aligned}&(\Delta\varphi_{s,i,j,n}\boldsymbol{k}_c\times{}^{S_C}\boldsymbol{r}^{Ei}_{j,n}-\Delta\varphi_{pi,j,n}\boldsymbol{k}_{pi}\times{}^{S_{Pi}}\boldsymbol{r}^{Ei}_{j,n}\\&-\sigma_{s,j}\boldsymbol{n}^{Ei}-\sigma_{pi,j}\boldsymbol{n}^{Ei}-\boldsymbol{\zeta}_i\times{}^{S_{Pi}}\boldsymbol{r}^{Ei}_{j,n})\cdot\boldsymbol{n}^{Ei}=\boldsymbol{\xi}_i\cdot\boldsymbol{n}^{Ei}\end{aligned} \tag{12b}$$

where $\boldsymbol{n}^{E/Ii}=\kappa_s(-\cos\beta\sin\psi_{E/Ii},\cos\beta\cos\psi_{E/Ii},\mp\sin\beta)^{\mathrm{T}}$ and $\psi_{E/Ii}=\psi_{pi}\mp\kappa_s\alpha_{E/I}$.

By solving Eq. (12), the deviation of the rotation angle relative to the ideal one in any slice-unit, $\Delta\varphi_{s,i,j,n}$ and $\Delta\varphi_{pi,j,n}$ can be obtained with consideration of 3D planet position errors and the tooth modifications.

3.1.3 Kinematical motion compatibility of slice-units

For the geometry and kinematics of a gear in the discrete PGT, at

DOI: XXX-XXX-XXXX

any instant, under ideal condition, every planet simultaneously meshes with the sun and ring gear with theoretical rotational angle, while under error condition, each slice-unit rotation angle deviates from ideal one. The deviation values of each slice-unit, $\Delta\varphi_{s,i,j,n}$ and $\Delta\varphi_{pi,j,n}$ obtained in above section satisfy contact condition Eq. (12). However, the motion of each slice-unit of a gear must cooperate with that of the gear body, i.e. $\Delta\varphi_{s,i,j,n}/\Delta\varphi_{pi,j,n}$ of each slice-unit should be compatible.

Assuming that each internal pair is engaged, and at least one slice-unit takes participate in meshing, the kinematic compatibility condition of each planet is written as

$$\Delta\varphi_{pi} = \min_{j,n}(-\kappa_s \Delta\varphi_{pi,j,n}) \ , \ n \in [1, n^{Ii}] \tag{13}$$

The sun gear meshes with at least one slice-unit of one planet for the sun gear floating, the kinematic compatibility condition of the sun gear satisfied,

$$\Delta\varphi_{s} = \min_{i,j,n}(\kappa_s \Delta\varphi_{s,i,j,n}) \ , \ n \in [1, n^{Ei}] \tag{14}$$

where $\Delta\varphi_{s,i,j,n}$ is obtained by the planets constraint, solving Eq.(12b) with $\Delta\varphi_{pi,j,n}=\Delta\varphi_{pi}$.

According to the kinematic compatibility condition, Eqs. (13)-(14), the contact situation for each slice-unit can be depicted by clearance (separation) between the slice-unit gear tooth pair. The clearance of the internal gear pair is

$$e_{j,n}^{Ii} = -\kappa_s r_{pi}(\Delta\varphi_{pi,j,n} - \Delta\varphi_{pi}) \tag{15}$$

The clearance of the external gear mesh is

$$e_{j,n}^{Ei} = \kappa_s r_{s}(\Delta\varphi_{s,i,j,n} - \Delta\varphi_{s}) \tag{16}$$

The discrete geometric and kinematic model considers duly the influence of 3D planet position errors and tooth modifications/errors on the mesh situation and rotation of gear pairs, which is used further in the load distribution analysis.

3.2 Discrete model with elastic deformation compatibility

Based on the discrete geometric and kinematic model, we go further to establish the discrete model under load condition, in which instantaneous meshing situations caused by 3D planet position errors, tooth modifications, elastic deformations and rigid body motions are coupled through the elastic deformation compatibility condition.

3.2.1 Elastic deformation compatibility condition

Under load condition, the elastic deformations of gear meshing pairs and those of the revolute pairs between each planet and carrier pin are considered. The elastic deformations will be compatible with the planet position errors or meshing clearances ($e_{j,n}^{E/Ii}$) caused by the position errors, tooth modifications, and the body motion displacements which has six-DOF, the translational displacement $\boldsymbol{x}_J=(x_{Jx}, x_{Jy}, x_{Jz})^{\mathrm{T}}$, and the rotational displacement $\boldsymbol{u}_J=(u_{Jx}, u_{Jy}, u_{Jz})^{\mathrm{T}}$ in $\boldsymbol{S}_C$ system $J=c, s, r$ and in $\boldsymbol{S}_{Pi}$ system $J=pi$.

The deformations of external and internal gear pairs and their motions are shown in Fig. 5. With the PGT running, the external and internal slice-unit gear pairs deform when their teeth are in contact, for which the elastic deformation compatibility along normal direction of engaged pair satisfies

$$\boldsymbol{\delta}_{j,n}^{E/Ii} = H \cdot \delta_{j,n}^{E/Ii} \boldsymbol{n}^{E/Ii}, \quad H = \begin{cases} 1 & \delta_{j,n}^{E/Ii} \geq 0 \\ 0 & \delta_{j,n}^{E/Ii} < 0 \end{cases} \tag{17a}$$

$$\delta_{j,n}^{E/Ii} = (\boldsymbol{x}_{s/r} - \boldsymbol{R}_{CPi}\boldsymbol{x}_{pi} + \boldsymbol{u}_{s/r} \times {}^{S_C}\boldsymbol{r}_{j,n}^{E/Ii} - \boldsymbol{R}_{CPi}\boldsymbol{u}_{pi} \times {}^{S_{Pi}}\boldsymbol{r}_{j,n}^{E/Ii}) \cdot \boldsymbol{n}^{E/Ii} - e_{j,n}^{E/Ii} \tag{17b}$$

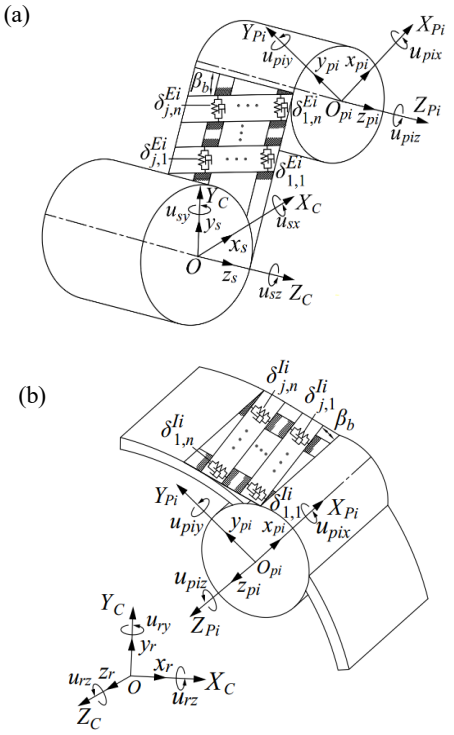

Fig. 5 Motion and deformation of gear pairs: (a) external gear pairs; (b) internal gear pairs

Each planet and carrier are bound by a revolute pair (R-pair) as shown in the Fig. 6. The elastic deformation compatibility of the R-pair of planet-carrier only relates to the linear translational deformation $\boldsymbol{\delta}_{cpi}$ and rotational deformation $\boldsymbol{\delta}_{cpi,u}$ along and about X_{pi}-, Y_{pi}-, Z_{pi}-axis , which can be expressed as

$$\begin{cases} \boldsymbol{\delta}_{cpi} = \boldsymbol{R}_{CPi}^{-1}\left(\boldsymbol{x}_c + \boldsymbol{u}_c \times \boldsymbol{a}_i\right) - \boldsymbol{x}_{pi} \\ \boldsymbol{\delta}_{cpi,u} = \boldsymbol{R}_{CPi}^{-1}\boldsymbol{u}_c - \boldsymbol{u}_{pi} \end{cases} \tag{18}$$

where $\delta_{cpi,uz}=0$ in $\boldsymbol{\delta}_{cpi,u}=(\delta_{cpi,ux}, \delta_{cpi,uz}, \delta_{cpi,uz})^{\mathrm{T}}$ due to the free motion about the Z-axis of R-pair.

Equation (17) describes the compatible condition between the deformations, meshing situations (clearances) and vibration displacements of each gear, or gear pair, and Eq. (18) describes that between the deformations, 3D position errors and vibration

displacements of planet-carrier. The elastic deformation compatibility conditions will be used to determine elastic force for each component under the interaction of the vibration displacement, error and elastic deformation.

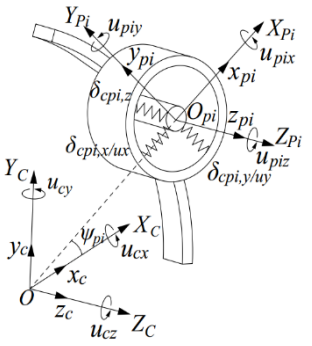

Fig. 6 Motion and deformation of the carrier and a planet gear

3.2.2 Time varying meshing stiffness of slice-unit pairs

The meshing stiffness of a gear is composed of bending stiffness *kb*, shear stiffness *ks*, axial compressive stiffness *ka* and contact stiffness *kh,* which can be calculated by the principle of potential energy based on the geometry and kinematics of gear meshing pair.[25,26]

The time varying meshing stiffness (TVMS) for the *j*-th slice unit, the *n*-th meshing pair can be obtained by

$$\frac{1}{k_{j,n}^{E/Ii}(t)}=\frac{1}{kh_{j,n}^{E/Ii}(t)}+\frac{1}{kb_{s/r,j,n}^{E/Ii}(t)}+\frac{1}{ks_{s/r,j,n}^{E/Ii}(t)}+\frac{1}{ka_{s/r,j,n}^{E/Ii}(t)}+\frac{1}{kb_{pi,j,n}^{E/Ii}(t)}+\frac{1}{ks_{pi,j,n}^{E/Ii}(t)}+\frac{1}{ka_{pi,j,n}^{E/Ii}(t)} \tag{19}$$

From Eq. (19) and elastic deformation of any slice-unit pair satisfying compatibility condition Eq. (17), meshing force of each slice-unit pair will be determined in the following discrete equilibrium formulations.

3.2.3 Discrete equilibrium formulations

Based on the equilibrium condition of each component with six-DOF, under the interaction of vibration displacements, errors and elastic deformations of each slice-unit, the discrete equilibrium formulations can be derived.

In each gear pair, there are meshing forces acting on the contact lines and torques on the gears. The meshing forces and torques at any instant can be determined by the summation of those of slice-units, by means of the elastic deformation satisfying compatibility equation and TVMS derived in the previous section. The forces are expressed in $\boldsymbol{S}_C$ or $\boldsymbol{S}_{Pi}$ system, as

$$\begin{cases}\boldsymbol{F}_J^{E/Ii}=-\sum_{j=1}^{n_l}\sum_{n=1}^{n^{E/Ii}}((k_{j,n}^{E/Ii}(t)\boldsymbol{\delta}_{j,n}^{E/Ii}(t)+c_{j,n}^{E/Ii}\dot{\boldsymbol{\delta}}_{j,n}^{E/Ii}(t))\\ \boldsymbol{T}_J^{E/Ii}=-\sum_{j=1}^{n_l}\sum_{n=1}^{n^{E/Ii}}({}^{S_J}\boldsymbol{r}_{j,n}^{E/Ii}\times(k_{j,n}^{E/Ii}\boldsymbol{\delta}_{j,n}^{E/Ii}+c_{j,n}^{E/Ii}\dot{\boldsymbol{\delta}}_{j,n}^{E/Ii}))\end{cases}\quad J=s,r \tag{20a}$$

$$\begin{cases}\boldsymbol{F}_{pi}^{E/Ii}=\boldsymbol{R}_{CPi}^{-1}\sum_{j=1}^{n_l}\sum_{n=1}^{n^{E/Ii}}((k_{j,n}^{E/Ii}(t)\boldsymbol{\delta}_{j,n}^{E/Ii}(t)+c_{j,n}^{E/Ii}\dot{\boldsymbol{\delta}}_{j,n}^{E/Ii}(t))\\ \boldsymbol{T}_{pi}^{E/Ii}=\boldsymbol{R}_{CPi}^{-1}\sum_{j=1}^{n_l}\sum_{n=1}^{n^{E/Ii}}({}^{S_{pi}}\boldsymbol{r}_{j,n}^{E/Ii}\times(k_{j,n}^{E/Ii}\boldsymbol{\delta}_{j,n}^{E/Ii}+c_{j,n}^{E/Ii}\dot{\boldsymbol{\delta}}_{j,n}^{E/Ii}))\end{cases} \tag{20b}$$

The equation of motion for the sun/ring gear in $\boldsymbol{S}_C$ system is

$$\boldsymbol{m}_J\ddot{\boldsymbol{q}}_J+(\boldsymbol{G}_J+\boldsymbol{c}_{J,h})\dot{\boldsymbol{q}}_J+(\boldsymbol{k}_{J,\omega}+\boldsymbol{k}_{J,h})\boldsymbol{q}_J+\sum_{i=1}^{N}\left(\boldsymbol{F}_J^{Ei},\frac{\boldsymbol{T}_J^{Ei}}{r_J}\right)^{\mathrm{T}}=\boldsymbol{F}_J \tag{21}$$

where $\boldsymbol{F}_s=(0,0,0,0,0,T_s/r_s)^{\mathrm{T}}$, $\boldsymbol{F}_r$=**0**, and $\boldsymbol{m}_J$, $\boldsymbol{q}_J$, $\boldsymbol{G}_J$, $\boldsymbol{c}_{J,h}$, $\boldsymbol{k}_{J,\omega}$, $\boldsymbol{k}_{J,h}$, *J=s, r, pi, c* are provided in Appendix. The equation of motion for carrier

$$\boldsymbol{m}_c\ddot{\boldsymbol{q}}_c+(\boldsymbol{G}_c+\boldsymbol{c}_{c,h})\dot{\boldsymbol{q}}_c+(\boldsymbol{k}_{c,\omega}+\boldsymbol{k}_{c,h})\boldsymbol{q}_c+\sum_{i=1}^{N}\left(\boldsymbol{F}_{pic},\frac{\boldsymbol{T}_{pic}}{a}\right)^{\mathrm{T}}=\boldsymbol{F}_c \tag{22a}$$

$$\boldsymbol{F}_c=(0,0,0,0,0,T_c/a)^{\mathrm{T}},\boldsymbol{F}_{pic}=-\boldsymbol{R}_{CPi}\boldsymbol{F}_{cpi},\boldsymbol{T}_{pic}=-\boldsymbol{R}_{CPi}\boldsymbol{T}_{cpi} \tag{22b}$$

The equation of motion for planet gears, considering the elastic deformation force of pin bearing $(\boldsymbol{F}_{cpi},\boldsymbol{T}_{cpi}/r_{pi})^{\mathrm{T}}$, internal and external meshing force in $\boldsymbol{S}_{Pi,,}$ is derived as

$$\boldsymbol{m}_{pi}\ddot{\boldsymbol{q}}_{pi}+\boldsymbol{G}_{pi}\dot{\boldsymbol{q}}_J+\boldsymbol{k}_{pi,\omega}\boldsymbol{q}_{pi}+\left(\boldsymbol{F}_{cpi},\frac{\boldsymbol{T}_{cpi}}{r_{pi}}\right)+\sum_{Mi=1}^{2}\left(\boldsymbol{F}_{pi}^{Mi},\frac{\boldsymbol{T}_{pi}^{Mi}}{r_{pi}}\right)^{\mathrm{T}}=0 \tag{23a}$$

where Mi=1, 2 expresses the planet *pi* meshing with internal and external gear (*Ei* and *Ii*) respectively. $\boldsymbol{F}_{cpi}$ and $\boldsymbol{T}_{cpi}$ are given as,

$$\begin{cases}F_{cpi,J}=k_{cpi,J}\delta_{cpi,J}+c_{cpi,J}\dot{\delta}_{cpi,J},\ J=x,y,z\\ T_{cpi,J}=k_{cpi,J}\delta_{cpi,J}+c_{cpi,J}\dot{\delta}_{cpi,J},\ J=ux,uy,uz\end{cases} \tag{23b}$$

By solving Eqs. (20)-(23), the motions and elastic deformations of each component, as well as the engagement forces of each gear pair can be determined.

So far the discrete model is developed. The model allows us to study the load distribution behaviors of a PGT by considering the influence of 3D planet position errors and tooth modifications. The load distribution coefficient, defined as the maximum actual load of all slice-units for the *i*-th internal pair versus the average value of all slice-units of all internal pairs in the PGT,[27] can be determined as

$$L_{pi}=\frac{F_{i,j\max}}{F_{\mathrm{avg}}}=\frac{\max_j\sum_{n=1}^{n^{Ii}}(k_{j,n}^{Ii}(t)\delta_{j,n}^{Ii}(t)+c_{j,n}^{Ii}\dot{\delta}_{j,n}^{Ii}(t))}{T_s/(N\cdot n_l\cdot r_s)} \tag{24}$$

4. Load distribution analysis

With the developed model, the load distribution of PGTs is analyzed. The parameters of one stage PGT in a wind turbine are shown

DOI: XXX-XXX-XXXX

in Table.1.

Table 1. The parameters of the PGT

Parameters	*Sun*	*Planet*	*Ring*	*Carrier*
Number of teeth N_J	22	41	104	
Normal modulus(mm)	16	16	16	
Mass m(kg)	466.7	473.4	2194.2	4392
Pressure angle α(deg)	20	20	20	
Helix angle β(deg)	7	7	7	
Support stiffness k(N/mm)	5×10^7	1×10^7	1×10^8	5×10^7
Torsional stiffness k_u(N/mm)	5×10^7	5×10^7	1×10^8	5×10^7
Damping c/c_u(N·s/mm)	10	10	10	10
Active face width l (mm)		380		
Center distance a(mm)		508		
Torque T_c(kNm)		1200		

4.1 Convergence of the discrete model

We look at first the convergence of the discrete model. It is tested by calculating the load distribution coefficient L_{p1} of four planet system, in which the PGT is divided into different slice-units up to 80, as shown in Fig. 7.

It can be seen from Fig. 7 that when the PGT is discretized into more than 60 slice-units, the L_{p1} tends to be stable state, which means that the solution of the discrete model is convergence. Hence, in our discrete model the PGT was divided into 60 slice-units.

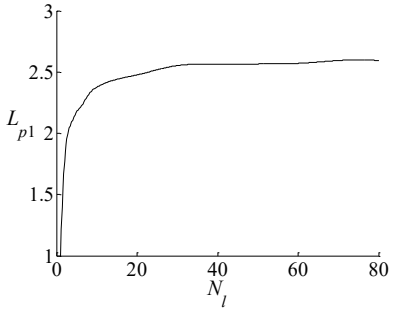

Fig. 7 Convergence of the discrete model

4.2 Load distribution coefficient with 3D planet position errors and tooth modifications

The tooth modification, including profile and longitudinal modification, is one of the most effective method to compensate the negative effects of errors. In this case study, the load distribution coefficient of the PGT with various 3D planet position errors and the lead crown modification is analyzed under the sun gear floating condition, due to the lead crown modification is the most effective for improving the load distribution which is performed by material removal near the tooth side edge and it possesses a smooth curve.[22] The parabola curve with the maximum deviation C is adopted as

$$\sigma_{J,j} = C\left(\frac{l/2-(j-1)\Delta l}{l/2}\right)^2 \quad J=s,pi,r,\ j=1,\ldots n_l \quad (25)$$

Using the proposed model in the Section 3, the contact force of one planet tooth of unit length for four-planet PGT system is calculated in a meshing cycle. Figure 8 shows the load distribution of the tooth surface from starting to leaving contact, in which the blue/red lines represent the double/triple tooth contact lines. Figure 8a shows the contact force under ideal condition, where the load distribution is unequal even without errors due to the gear deflection caused by axial force. Under the angular misalignment (3D) error condition, the edge contact exists and the maximum load distributes at the edge shown as Fig. 8b. With lead modification, the edge contact is removed, and the maximum load has moved to the middle of tooth width decreased from 1173N/mm to 887N/mm.

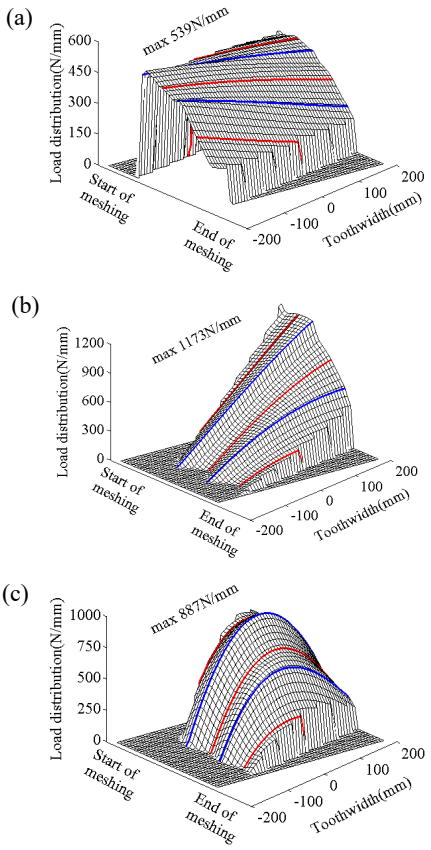

Fig. 8 Contact force of unit length with four planets: (a) ideal condition; (b) with angular misalignment error $\zeta_r l$=40μm; (c) with angular misalignment error $\zeta_r l$=40μm and lead modification C=10μm.

To investigate the influence of 3D planet position errors and modification parameter C on the load distribution coefficient, the load distribution coefficient of the three-planet and four-planet PGT with planet-1 position errors is calculated by using Eq. (24). With parallel tangential misalignment and lead crown modification, the load distribution coefficient of the three- and four-planet system are shown in Fig. 9. For three-planet system, the load distribution coefficient with or without modification is independent of parallel misalignment for floating sun gear, and the modification worsen the load distribution behavior. For four-planet system, the influence of parallel tangential misalignment on load distribution coefficient presents linear relationship and the influence of parallel tangential misalignment on load distribution coefficient of opposed planet gears

is equal.

The angular misalignment, in radial ζ_r and tangential ζ_t, will cause the edge contact and the diverse mesh condition of each slice-unit pair. For convenience, the angular position error is converted to linear one through multiplying width of the gear l, i.e. $\zeta_t l$ and $\zeta_r l$.

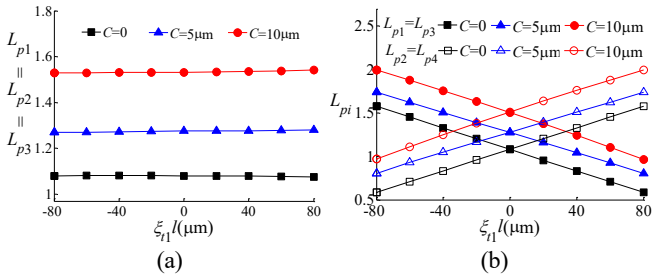

Fig. 9 The load distribution coefficient L_{pi} with parallel tangential misalignment ξ_{t1}: (a) three-planet system; (b) four-planet system

The influence of tangential angular misalignment ζ_t on the load distribution coefficient is analyzed as shown in Fig.10. The relationship between load distribution coefficient and tangential angular misalignment is linear without modification and nonlinear with modification, which is asymmetrical for the gear deflection. The lead crown modification improves the load distribution behavior for the planet with tangential angular misalignment and the preferable deviation is C=5μm.

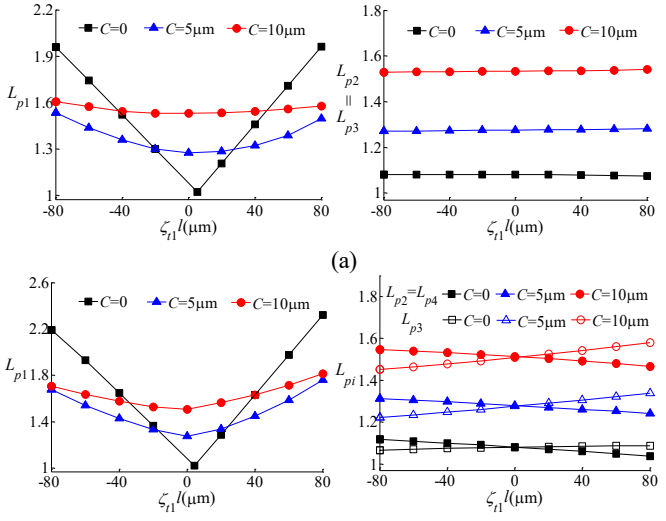

Fig. 10 The load distribution coefficient L_{pi} with tangential angular misalignment ζ_{t1}: (a) three-planet system; (b) four-planet system

The influence of radial angular misalignment ζ_r on the load distribution coefficient is shown in Fig. 11. For a four-planet system with the same error magnitude ξ_t=$\zeta_t l$=$\zeta_r l$=−40μm, the load distribution coefficient of *plant*-1 is 1.329, 1.649 and 2.408 respectively. The sensitivity of the tangential angular misalignment ζ_t to the load distribution coefficient is less than the radial one ζ_r but the same level for the parallel tangential misalignment ξ_t. In addition, the sensitive direction for parallel misalignment is only tangential but both of radial and tangential direction for the angular misalignment. The load distribution coefficient is much sensitive to radial angular misalignment.

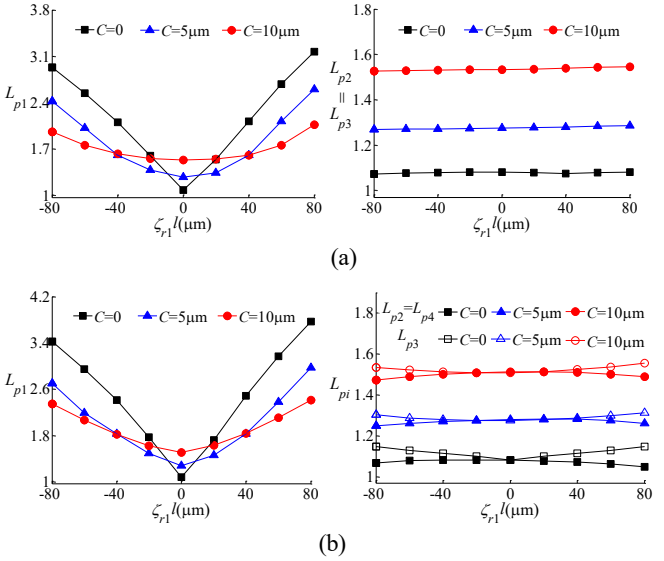

Fig. 11 The load distribution coefficient L_{pi} with radial angular misalignment ζ_{r1}: (a) three-planet system; (b) four-planet system

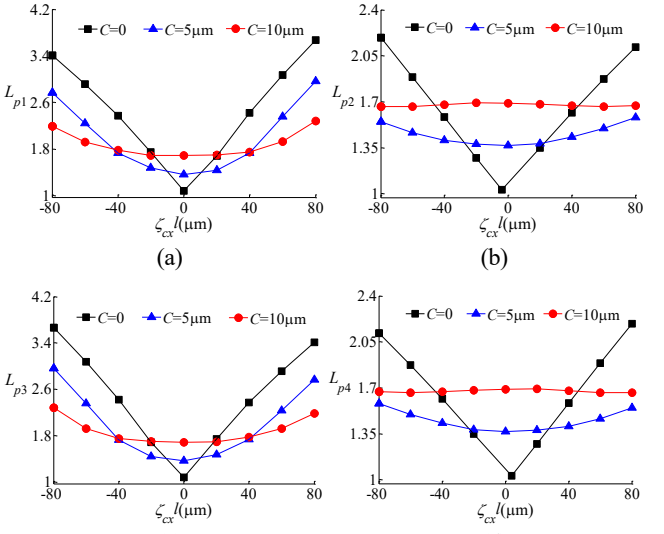

Fig. 12 The load distribution coefficient L_{pi} with angular misalignment errors ζ_{cx}: (a) L_{p1}; (b) L_{p2}; (c) L_{p3}; (d) L_{p4}

Figure 12 shows cases when all planets are endowed with the angular misalignment errors ζ_{cx} about the X-axis of the carrier frame $\boldsymbol{S}_C$ which can be converted to ζ_r and ζ_t in $\boldsymbol{S}_{Pi}$. The amplitudes of L_{p1} and L_{p3} are almost consistent which are larger than that of L_{p2} and L_{p4} for radial misalignment under the effect of ζ_{cx}.

It can be observed from Figs. 9 to 12 that the suitable tooth modification can improve the load distribution. The preferable amount of tooth modification is depended on the type and magnitude of the planet position errors. To further illustrate how the amount of tooth modification affects the load distribution behavior with distinct type and magnitude of the planet position errors, some load distribution coefficients of a four-planet system are summarized in Table 2. For the PGT with only parallel misalignment error, the

DOI: XXX-XXX-XXXX

modification worsens the load distribution behavior, which suggests any modification is not really needed. For the PGT with angular misalignment errors, the preferable modification deviation is C=5μm with tangential angular misalignment more than 20μm or radial angular misalignment errors less than 40μm (L_{p1}=1.447/1.585/1.761 with $\zeta_{t1}l$=40/60/80μm, L_{p1}=1.462/1.825 with $\zeta_{r1}l$ =20/40μm). Otherwise, the preferable modification deviation is C=10μm if the radial angular misalignment error $\zeta_r l$ is more than 40μm (L_{p1}=2.107/2.413 with $\zeta_{r1}l$=60/80μm). It shows that the preferable modification is different for distinct type and magnitude of planet position errors.

Table 2. Load distribution coefficients of a four-planet system with distinct tooth modification and type/magnitude planet position errors

Type/magnitude of errors(μm)		L_{p1} with C=0μm	L_{p1} with C=5μm	L_{p1} with C=10μm
ξ_{t1}	20	0.956	1.161	1.378
	40	0.832	1.045	1.244
	60	0.708	0.926	1.107
	80	0.584	0.802	0.964
$\zeta_{t1}l$	20	1.288	1.336	1.566
	40	1.633	1.447	1.630
	60	1.977	1.585	1.715
	80	2.322	1.761	1.813
$\zeta_{r1}l$	20	1.722	1.462	1.629
	40	2.489	1.825	1.833
	60	3.165	2.379	2.107
	80	3.767	2.968	2.413

5. Load distribution testing

The load distribution tests were conducted on a helical PGT of the wind turbine power system with rated power 2MW, input velocity 15rpm and air density 1.23kg/m^3, where three and four planet gears are tested. The parameters are in Table 1, and the lead modification C=7.5μm which is designed according to analysis in the section 4.2.

5.1 Testing setup

Figure 13 shows the setup for testing PGTs performance under load operating condition. Two opposing PGTs and two driving motors are employed to provide jointly a driving torque up to 1200kNm.

In total, N groups of strain gauges located on the ring gear uniformly to determine the load distribution coefficient. In each group, two rows of eight strain gauges are stuck on the tooth roots along the tooth width direction shown in Fig. 14. The strain gauge data is collected by the data acquisition system of Vishay 7000-128-SM strain indicator with 128 channels.

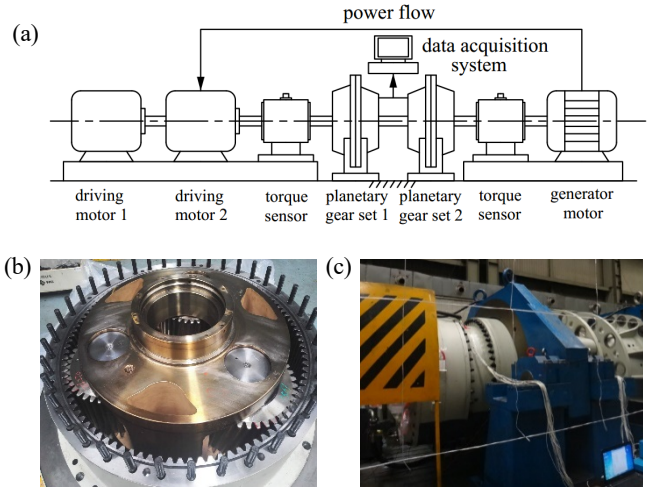

Fig. 13 The testing setup for wind turbine PGTs: (a) layout schematic; (b) view of a PGT with cover removed; (c) photo of testing setup

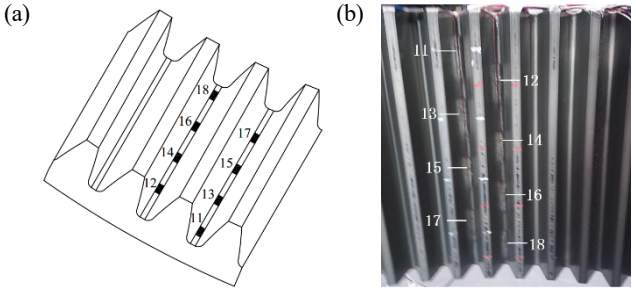

Fig. 14 Strain gauge location of the first group for load distribution test: (a) the first group of strain gauges location; (b) close-up view

5.2 Testing procedure and data processing

The actual 3D planet position errors were obtained by measuring the carrier pinholes locations using 3D measuring instruments before the PGT assembling. The errors are listed in in Table 3.

Table 3. The actual 3D planet position errors of carrier pinholes

Measured errors(μm)		ξ_r	ξ_t	$\zeta_r l$	$\zeta_t l$
Three-planet system	Planet-1	-1	3	24	19
	Planet-2	-25	-25	4	-20
	Planet-3	4	6	28	-16
Four-planet system	Planet-1	-16	-2	-2	28
	Planet-2	13	-18	9	16
	Planet-3	-1	-34	-4	-8
	Planet-4	-16	-20	-16	-12

The test of the load distribution are conducted under the carrier speed 15rpm with four load conditions, i.e. 25%, 50%, 75% and 100% rated torque T_c respectively. Under each stable operating load condition, the strain gauge peak-to-peak values with the carrier 20 rotating circles are recorded which form the $\lambda \times N$ matrix as[18]

$$\begin{array}{c|c|c} \text{first group} & \text{second group} & N\text{th group} \\ \left[\begin{array}{ccc} {}_1\varepsilon_{p1}^1 & \cdots & {}_1\varepsilon_{p1}^8 \\ {}_2\varepsilon_{pN}^1 & \cdots & {}_2\varepsilon_{pN}^8 \\ \vdots & & \\ {}_\lambda\varepsilon_{p2}^1 & \cdots & {}_\lambda\varepsilon_{p2}^8 \end{array}\right. & \left.\begin{array}{ccc} {}_1\varepsilon_{p2}^1 & \cdots & {}_1\varepsilon_{p2}^8 \\ {}_2\varepsilon_{p1}^1 & \cdots & {}_2\varepsilon_{p1}^8 \\ \vdots & & \\ {}_\lambda\varepsilon_{p3}^1 & \cdots & {}_\lambda\varepsilon_{p3}^8 \end{array}\right. & \left.\begin{array}{ccc} {}_1\varepsilon_{pN}^1 & \cdots & {}_1\varepsilon_{pN}^8 \\ {}_2\varepsilon_{p(N-1)}^1 & \cdots & {}_2\varepsilon_{p(N-1)}^2 \\ \vdots & & \\ {}_\lambda\varepsilon_{p1}^1 & \cdots & {}_\lambda\varepsilon_{p1}^8 \end{array}\right] \end{array} \quad (26)$$

where $\lambda=20N$ is the number of peak-to-peak values for each group.

The measured load distribution coefficient is defined as the mean value of the maximum peak-to-peak microstrain for the i-th planet versus the average for all planets, since the peak-to-peak values represent different forces acting on each planet with carrier rotation, as

$$L_{pi}=\frac{1}{\lambda}\sum_{d=1}^{\lambda}\frac{{}_d\varepsilon_{i\max}}{{}_d\varepsilon_{\text{avg}}}=\frac{1}{\lambda}\sum_{d=1}^{\lambda}\frac{\max_k {}_d\varepsilon_{pi}^k}{\sum_{i=1}^{N}\sum_{k=1}^{8}{}_d\varepsilon_{pi}^k/8N} \quad (27)$$

5.3 Results analysis

The strain gauge raw data with the carrier two rotating circles at the edge and middle position (1 and 4) of the first group is shown in Fig. 15. The micro strain at the middle position is obvious larger than that of edge position due to the lead modification.

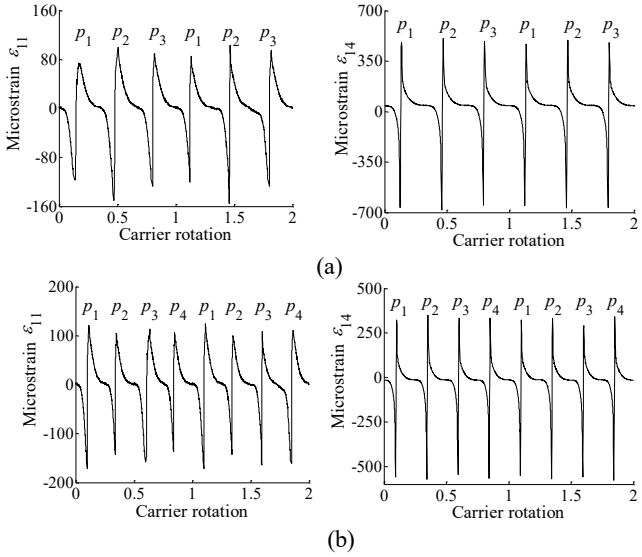

Fig. 15 The raw data curves at position 1 and 4 of the first group: (a) three-planet system; (b) four-planet system

The strain gauge peak-to-peak values of the first group with the carrier five rotating circles is shown in Fig. 16. The average of $\varepsilon_{11}/\varepsilon_{18}$ (1st/8th strain gauge micro strain of the first group) for three and four-planet system are 226/484 and 257/157 respectively, by which obvious angular misalignment phenomenon can be observed. The micro strain of the strain gauge is largest in the middle of tooth width although the angular misalignment errors exist and decreases rapidly along the longitude direction clarifying the effects of tooth modifications.

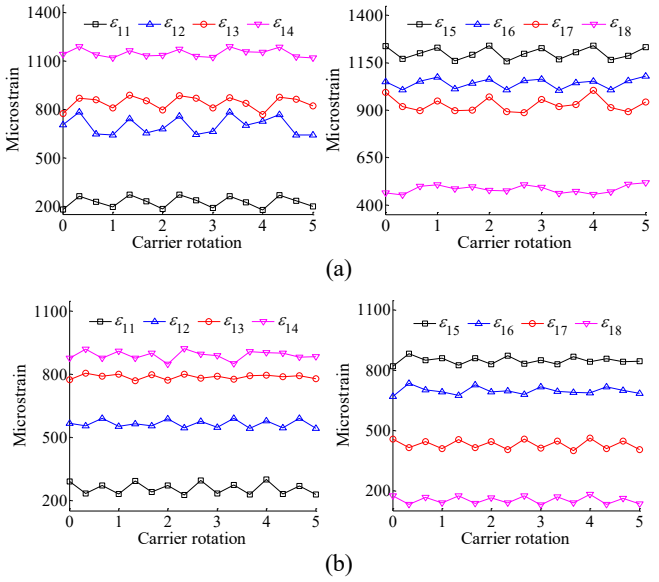

Fig. 16 The strain gauge peak-to-peak values of the first group: (a) three-planet system; (b) four-planet system

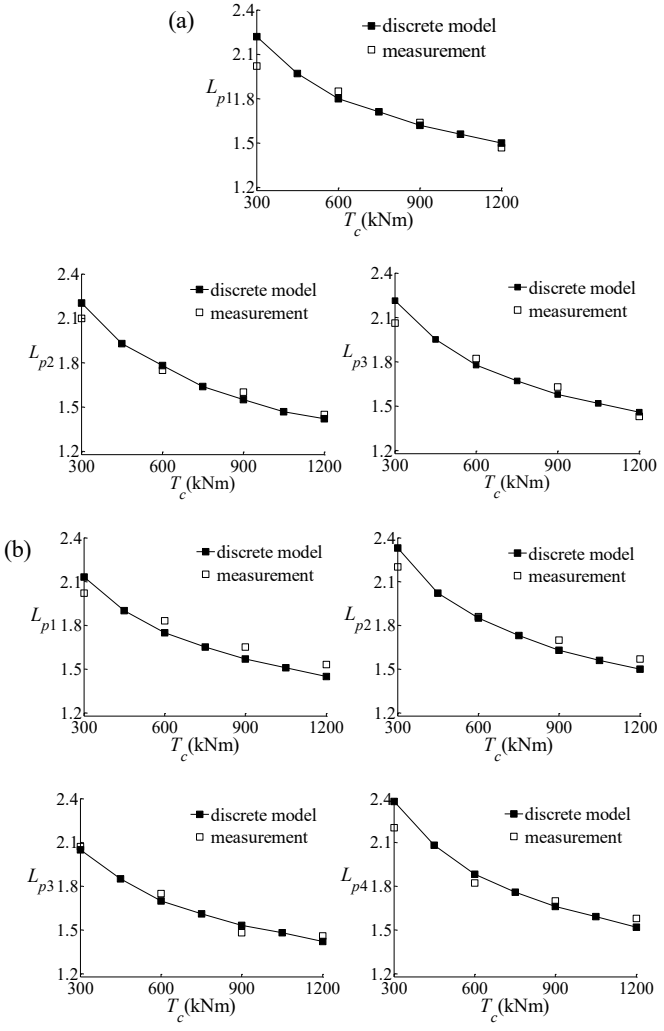

Fig. 17 The load distribution coefficient L_{pi} obtained by the discrete model and experiment: (a) three-planet system; (b) four-planet system

The load distribution coefficients obtained by the discrete model

DOI: XXX-XXX-XXXX

and the experiment results for three- and four-planet system are shown in Fig. 17. There is a good agreement between the load distribution coefficients obtained from two approaches. The deviation of the load distribution coefficients between the calculated and experiment results are calculated, in which the average deviations of three- and four-planet system are in 3.9% and 4.6%, respectively, and the maximum deviation is 10.9% and 9.1%, respectively. It may be understood and reasonable due to some unknown factors exist in the actual PGTs. The comparison verifies the accuracy of the discrete model for load distribution analysis.

6. Conclusions

This paper presents a new load distribution analysis method with consideration of 3D planet position errors and tooth modifications. The method is developed upon a discrete model, which simplifies the 3D gear dynamics modeling. The proposed model is rigorous and versatile, which considers duly the influence of 3D planet position errors and tooth modifications on instantaneous meshing situation, and elastic deformation of each gear pair, and then on the dynamics forces in a PGT system with arbitrary planet gears through developed compatibility conditions.

Using the proposed method, simulations were conducted to analyze the influence of 3D planet position errors and tooth modifications contribution to the load distribution of a helical PGT. The simulations illustrate that the angular planet position errors, both in radial and tangential direction, affect the load distribution behavior which cannot be ignored and the influence of radial angular misalignment error on load distribution is highest. Moreover, the tooth modification improves the load distribution behavior and the suitable modification is depends on the type and magnitude of the planet position errors.

Tests of load distribution were conducted on PGTs, one having three and the other four planets. Results show good agreement between the simulation and tests for both PGTs, which validates the proposed method.

The experimentally validated model allows its further application in load analysis of other planet gear train systems. The model can also be used in design optimization of gear tooth profile, bearing stiffness design and position error determination to achieve optimum load distribution. In this regard, optimization techniques, such as topology optimization [ref], Gradient search method with Kalman Filter [ref], and particle swarm optimization [ref], etc, can be utilized, which is a topic of future study.

ACKNOWLEDGEMENT

This work is financially supported by the National Natural Science Foundation of China (No. 51375065)

APPENDIX

The transformation matrix from $\boldsymbol{S}_{Pi}$ to $\boldsymbol{S}_C$ is

$$\boldsymbol{M}_{CPi}=\begin{pmatrix}\cos\psi_{pi} & -\sin\psi_{pi} & 0 & a\cos\psi_{pi}\\ \sin\psi_{pi} & \cos\psi_{pi} & 0 & a\sin\psi_{pi}\\ 0 & 0 & 1 & 0\\ 0 & 0 & 0 & 1\end{pmatrix} \tag{A-1}$$

The mass and displacement matrixes are

$$\begin{aligned}&\boldsymbol{m}_J=diag(m_J,m_J,m_J,I_{Jx}/r_J^2,I_{Jy}/r_J^2,I_{Jz}/r_J^2),\ r_c=a\\ &\boldsymbol{q}_J=(x_{Jx},x_{Jy},x_{Jz},u_{Jx},u_{Jy},u_{Jz})^{\mathrm{T}},\ J=c,s,pi,r\end{aligned} \tag{A-2}$$

The gyroscopic matrix is

$$\boldsymbol{G}_J=\omega_c\begin{pmatrix}\boldsymbol{m}_m & \boldsymbol{0}\\ \boldsymbol{0} & \boldsymbol{m}_I\end{pmatrix},\ \boldsymbol{m}_{m/I}=\begin{pmatrix}0 & -b_{m/I} & 0\\ b_{m/I} & 0 & 0\\ 0 & 0 & 0\end{pmatrix} \tag{A-3}$$

$$b_m=2m_J,b_I=I_{Jy}/r_J^2,\ J=c,s,pi,r$$

The centripetal and supporting stiffness matrixes are

$$\boldsymbol{k}_{J,\omega}=-m_J\omega_c^2\cdot diag(1,1,0,0,0,0),\ J=c,s,pi,r \tag{A-4}$$

$$\boldsymbol{k}_{J,h}=diag(k_J,k_J,k_J,k_{Ju},k_{Ju},k_{Ju}),\ J=c,s,r \tag{A-5}$$

$$\boldsymbol{c}_{J,h}=diag(c_J,c_J,c_J,c_{Ju},c_{Ju},c_{Ju}),\ J=c,s,r \tag{A-6}$$

REFERENCES

1. Singh A., "Application of a System Level Model to Study the Planetary Load Sharing Behavior," Journal of Mechanical Design, Vol. 127, No. 3, pp. 469-476, 2005.
2. Ge N., Zhang J., "Finite Element Analysis of Internal Gear in High-Speed Planetary Gear Units," Transactions of Tianjin University, Vol. 14, No. 1, pp. 11-15, 2008.
3. Saada A., Velex P., "An Extended Model for the Analysis of the Dynamic Behavior of Planetary Trains," Journal of Mechanical Design, Vol. 117, No. 2, pp. 241-247, 1995.
4. Kahraman A., "Load Sharing Characteristics of Planetary Transmissions," Mechanism and Machine Theory, Vol. 29, No. 8, pp. 1151-1165, 1994.
5. Toda A, Botman M., "Planet Indexing in Planetary Gears for Minimum Vibration," ASME Paper No 79-DET-73, 1979.
6. Bodas A, Kahraman A., "Influence of Carrier and Gear Manufacturing Errors on the Static Load Sharing Behavior of Planetary Gear Sets," JSME International Journal, Series C, Vol. 47, pp. 908-915, 2004.
7. Gu X., Velex P., "A Dynamic Model to Study the Influence of Planet Position Errors in Planetary Gears," Journal of Sound and Vibration, Vol. 331, No. 20, pp. 4554-4574, 2012.

8. Singh A., "Load Sharing Behavior in Epicyclic Gears: Physical Explanation and Generalized Formulation," Mechanism and Machine Theory, Vol. 45, pp. 511-530, 2010.
9. Singh A., "Application of a System Level Model to Study the Planetary Load Sharing Behavior," Journal of Mechanical Design, Vol. 127, pp. 469-476, 2005.
10. Dong H., Wu Y., Wang D., Bai S., "M-DOF Dynamic Model for Load Sharing Behavior Analysis of PGT," Journal of Mechanical Science and Technology, Vol. 30, No. 3, pp. 993-1001, 2016.
11. Hu Y., Talbot D., Kahraman A., "A Load Distribution Model for Planetary Gear Sets," Journal of Mechanical Design, Vol. 140, pp. 1-14, 2018.
12. Ren F., Qing D., Lim T.C., "Study on Dynamic Characteristics and Load Sharing of a Herringbone Planetary Gear with Manufacturing Errors," International Journal of Precision Engineering and Manufacturing, Vol. 15, No. 9, pp. 1925-1934, 2014.
13. Kim J.-G, Park Y.-J, Lee S.-D, Kim J.-H, "Influence of the Carrier Pinhole Position Errors on the Load Sharing of a Planetary Gear Train," International Journal of Precision Engineering and Manufacturing, Vol. 19, No. 4, pp. 537-543, 2018.
14. Park Y., Lee G., Oh J., et al., "Effects of Non-torque Loads and Carrier Pinhole Position Errors on Planet Load Sharing of Wind Turbine Gearbox," International Journal of Precision Engineering and Manufacturing-Green Technology, Vol. 6, No. 2, pp. 281-292, 2019.
15. Cao Z., Shao Y., Zuo MJ., et al., "Dynamic and Quasi-Static Modeling of Planetary Gear Set Considering Carrier Misalignment Error and Varying Line of Action along Tooth Width," Proc IMech Part C: J Mechanical Engineering Science, Vol. 229, No. 8, pp. 1348-1360, 2015.
16. Abousleiman V., Velex P., "A Hybrid 3D Finite Element/Lumped Parameter Model for Quasi-Static and Dynamic Analyses of Planetary/Epicyclic Gear Sets," Mechanism and Machine Theory, Vol. 41, No. 6, pp. 725-748, 2006.
17. Zhang J., Song Y., Wang J., "Dynamic Modeling for Spur Planetary Gear Transmission with Flexible Ring Gear," Journal of Mechanical Engineering, Vol. 45, No. 12, pp. 29-36, 2009.
18. Ligata H., Kahraman A., Singh A., "An Experimental Study of the Influence of Manufacturing Errors on the Planetary Gear Stresses and Planet Load Sharing," Journal of Mechanical Design, Vol. 130, No. 4, pp. 137-139, 2008..
19. Kim J.-G, Park Y.-J, Lee G.-H, et al., "An Experimental Study on the Effect of Carrier Pinhole Position Errors on Planet Gear Load Sharing," International Journal of Precision Engineering and Manufacturing, Vol. 17, No.10, pp. 1305-1312, 2016.
20. Kim J.-G, Park Y.-J, Lee G.-H, et al., "Experimental Study on the Carrier Pinhole Position Error Affecting Dynamic Load Sharing of Planetary Gearboxes," International Journal of Precision Engineering and Manufacturing, Vol. 19, No.6, pp. 881-887, 2018.
21. Litvin F. L., Vecchiato D., Demenego A., et al., "Design of One Stage Planetary Gear Train with Improved Conditions of Load Distribution and Reduced Transmission Errors," Journal of Mechanical Design, Vol. 124, No. 4, pp. 745-752, 2002.
22. Mohamad E., Komori M., Murakami H., et al., "Analysis of General Characteristics of Transmission Error of Gears with Convex Modification of Tooth Flank Form Considering Elastic Deformation under Load," Journal of Mechanical Design, Vol. 13, No. 6, pp. 2751-2764, 2009.
23. Oh S., Oh S., Kang J., "A Study on Modeling and Optimization of Tooth Microgeometry for a Helical Gear Pair," International Journal of Precision Engineering and Manufacturing, Vol. 14, No. 3, pp. 423-427, 2013.
24. Kim J., Park N., Lee H., "Tooth Modification for Optimizing Gear Contact of a Wind-Turbine Gearbox," Proc IMech Part C: J Mechanical Engineering Science, Vol. 230, No. 7, pp. 1318-1330, 2016.
25. Wang Q., Zhang Y., "A Model for Analyzing Stiffness and Stress in a Helical Gear Pair with Tooth Profile Errors," Journal of Vibration and Control, Vol. 23, No. 10, pp. 272-289, 2015.
26. Liang X., Zuo M., Guo Y., "Evaluating the Time-Varying Mesh Stiffness of a Planetary Gear Set Using the Potential Energy Method," Proc IMech Part C: J Mechanical Engineering Science, Vol. 228, No. 3, pp. 535-547, 2014.
27. Zhou C., Chen C., Gui L., et al., "A Nonlinear Multi-Point Meshing Model of Spur Gears for Determining the Face Load Factor," Mechanism and Machine Theory, Vol. 126, pp. 210-224, 2018.